# Systematic failure of the Woods-Saxon nuclear potential to describe both fusion and elastic scattering: Possible need for a new dynamical approach to fusion

J. O. Newton, R. D. Butt, M. Dasgupta, D. J. Hinde, I. I. Gontchar,* and C. R. Morton
*Department of Nuclear Physics, Research School of Physical Sciences and Engineering, Australian National University, Canberra, ACT 0200, Australia*

K. Hagino
*Yukawa Institute for Theoretical Physics, Kyoto University, Kyoto 606-8502, Japan*
(Received 21 December 2003; published 30 August 2004)

A large number of precision fusion excitation functions, at energies above the average fusion barriers, have been fitted using the Woods-Saxon form for the nuclear potential in a barrier passing model of fusion. They give values for the empirical diffuseness parameter $a$ ranging between 0.75 and 1.5 fm, compared with values of about 0.65 fm which generally reproduce elastic scattering data. There is a clear tendency for the deduced $a$ to increase strongly with the reaction charge product $Z_1Z_2$, and some evidence for the effect of nuclear structure on the value of $a$, particularly with regard to the degree of neutron richness of the fusing nuclei, and possibly with regard to deformation. The measured fusion-barrier energies are always lower than those of the bare potentials used, which is expected as a result of adiabatic coupling to high energy collective states. This difference increases with increasing $Z_1Z_2$ and calculations show that about 1/3 of it may be attributed to coupling to the isoscalar giant-quadrupole resonances in the target and projectile. Coupling to all giant resonances may account for a significant part. Fluctuations about the trend line may be due to systematic errors in the data and/or structure effects such as coupling to collective octupole states. Previously suggested reasons for the large values of $a$ have been related to departures from the Woods-Saxon potential and to dissipative effects. This work suggests that the apparently large values of $a$ may be an artifact of trying to describe the dynamical fusion process by use of a static potential. Another partial explaination might reside in fusion inhibition, due for example to deep-inelastic scattering, again a process requiring dynamical calculations.

DOI: 10.1103/PhysRevC.70.024605 PACS number(s): 25.70.Jj, 24.10.Eq, 21.60.Ev, 27.60.+j

## I. INTRODUCTION

Measurements of fusion-barrier distributions, through precisely determined fusion excitation functions [1–3], have been carried out for more than a decade. They have provided an experimental demonstration of the expectation [4] that the simple one-dimensional potential barrier for fusion effectively splits into a distribution of barriers by dynamical coupling to collective modes in the target and projectile nuclei. Both simplified [5–7] and realistic [8,9] coupled channels codes have been used, often successfully, in reproducing experimental fusion-barrier measurements. In general, the measurements are of capture cross sections rather than fusion cross sections, since they do not distinguish between fission and quasifission [10] or complete and incomplete fusion. In this paper, the cross sections will be referred to in the usual way as fusion cross sections. Nevertheless, these cross sections can be appropriately described by a barrier passing model. For such calculations it has been usual to take an energy independent Woods-Saxon form for the real nuclear potential,

$$V_N(r) = -V_0/\{1+\exp[(r-r_0A_1^{1/3}-r_0A_2^{1/3})/a]\}, \qquad (1)$$

where $A_1$ and $A_2$ are the mass numbers of the projectile and target nuclei, $V_0$ is the depth, $r_0$ is the radius parameter, and $a$ is the diffuseness parameter. When combined with the Coulomb potential, this results in a potential barrier referred to as the fusion barrier. For zero angular momentum the fusion barrier is characterized by its energy $V_B$, radius $R_B$, and curvature at $R_B$ which, in the parabolic barrier approximation, is identified with $\omega$, the oscillator frequency of the inverted parabolic barrier.

The shapes of the barrier distributions can usually be understood and fairly well reproduced by coupling to known collective modes such as vibration, and rotation for deformed nuclei, and to nucleon transfer [3]. However, some aspects are still not understood. For example, it has not been possible to simultanously reproduce the barrier distribution and the fusion cross sections well above and below the average barrier for the $^{16}O+^{208}Pb$ reaction [11]. To reproduce the above-barrier cross sections required $a=1.0$ fm; however, the barrier distribution could not be reproduced unless a smaller value of $a\simeq 0.4$ fm was used. It might be expected that a reaction involving two very well studied double closed-shell nuclei would be one of the easiest to reproduce with a coupled channels calculation. However, the reverse is the case, this being one of the most poorly reproduced reactions of those studied so far. Notwithstanding the $^{16}O+^{208}Pb$ case, good descriptions of both cross sections and barrier distributions can be made, with identical values of $a$, for many other reactions. However, to obtain such good results a diffuseness $a\approx 1$ fm or higher is often required.

In contrast to the fusion results, elastic scattering cross sections can generally be well reproduced by a Woods-Saxon

*Permanent address: Omsk State Transport University, pr. Marksa 35, Omsk RU-644046, Russia.

 

nuclear potential with $a \approx 0.65$ fm, $r_0 \approx 1.18$ fm, and $V_0 \approx 65$ MeV [12,13]. The parameters of these potentials were obtained from a least-squares fit to experimental data while requiring that the maximum force $\partial V_N(r)/\partial r$ corresponds to that given by the proximity potential [14]. Elastic scattering and fusion differ in that they explore different regions of the nuclear potential, the former involving much larger separation distances than the latter. One possible reason for the differences in $a$ might be that the nuclear potential departs from the Woods-Saxon (WS) form at closer distances.

The nuclear potential can in principle be calculated with the double-folding model, which might be thought to be more realistic than the phenomenological Woods-Saxon potential. For the case of $^{16}O+^{208}Pb$, it was shown [15] that, near the barrier radius, this potential roughly follows the Woods-Saxon potential which fits the elastic data and thus cannot reproduce the fusion excitation function. Therefore use of the double-folding model does not resolve the problem of $^{16}O+^{208}Pb$. A recent calculation [16] of double-folding potentials, using density-dependent M3Y parametrizations based on the Paris and Reid nucleon-nucleon interactions, has also reached similar conclusions for a variety of systems. Furthermore, it was shown that the calculated fusion-barrier heights are smaller than those experimentally observed, contrary to what would be expected for a bare potential (see Sec. III A). The double-folding model may not be appropriate for fusion as it is based on the frozen density approximation, in which it is assumed that the reaction takes place much faster than the dynamical density evolution, i.e., that the densities of the target and projectile nuclei remain unchanged at all distances. This must be invalid at short distances where the overlap density exceeds the saturation density $\rho_0$, and the validity may also be questioned at separations corresponding to the fusion-barrier radius, where the overlap density is $\approx 0.25\rho_0$.

Another possible explanation of the large apparent diffuseness might result from the effect of energy dissipation, which is also related to density variations during the collision process, and suggests the necessity of dynamical calculations [15]. So far no attempt has been made to perform a systematic study of how the parameter $a$, required to fit fusion data, varies with reaction properties and nuclear structure. In this paper we have chosen to compare the results against the charge product $Z_1Z_2$, which is related to the strength of the Coulomb potential at the fusion-barrier radius. The higher the value of the Coulomb potential at the barrier, the closer is the barrier radius to the sum of the half-density radii of target and projectile nuclei. This is because the nuclear force, as a function of separation distance, is expected to be fairly independent of charge or mass. The higher the summed density of target and projectile at the barrier, the more likely are dissipative effects to be important. Similar trends are found by plotting the results as a function of $A_1^{1/3}+A_2^{1/3}$. This study has been made in the expectation that it may suggest explanations for the anomaly and stimulate further lines of investigation. Selected results from this work have already been presented [17]

## II. ANALYSIS, PROCEDURES, AND CONSTRAINTS

Fusion cross sections at energies above the highest barrier and below the lowest barrier in the distribution might be expected to depend principally on the nuclear potential. Therefore it would be interesting to see whether the same value of $a$ is required to fit both the low and high energy data. However, cross sections below the lowest barrier are very small and difficult to measure. At present there are insufficient data in this region to include in a systematic survey. In a recent publication on the reaction $^{60}Ni+^{89}Y$, Jiang *et al.* [18,19] have suggested that, at bombarding energies below about $0.91V_B$, the rate of fall of $\sigma_{fus}$ with decreasing bombarding energy becomes greater than that predicted by calculations (they claim similar results for the reactions $^{58}Ni+^{58}Ni$ [20], $^{90}Zr+^{89}Y$, $^{90}Zr$, $^{92}Zr$ [21], and $^{64}Ni+^{64}Ni$ [22]). Hagino *et al.* [23] pointed out that, at extreme sub-barrier energies ($\sigma_{fus}$ down to the $10^{-4}$ mb level), it is necessary to make an exact calculation of the barrier penetrability, rather than one based on the parabolic barrier approximation, and, furthermore, that the large values of $a$ required to fit the above-barrier cross sections significantly affect the sub-barrier cross sections. Further measurements at deep sub-barrier energies would be of great value in elucidating this matter. Because of the limited availability of deep sub-barrier data, the present study is confined to fusion cross sections $\sigma_{fus}$ above the average fusion barrier, which were fitted to obtain the parameters of the Woods-Saxon potential.

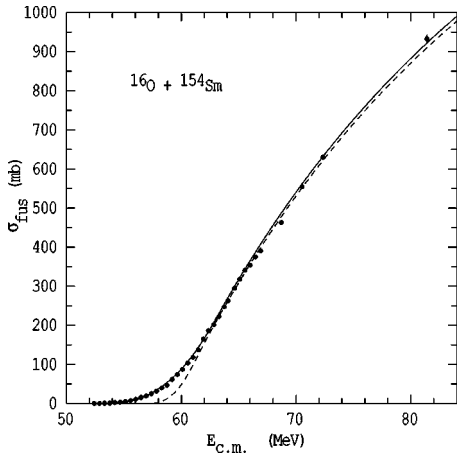


FIG. 1. The effect of coupling on fusion cross sections. Calculations with the realistic coupled channels code CCFULL, using the same potential parameters derived from fitting the above-barrier data, are shown for the $^{16}O+^{154}Sm$ reaction. The dashed line is for no coupling and the full line for coupling to rotational states in the strongly deformed $^{154}Sm$ nucleus. There is little difference between the slopes of the two curves for $\sigma_{fus}$ above about 200 mb, but a major difference in the barrier region. Here only the coupled channels calculation gives a reasonable fit to the data, shown by the filled circles [2].

### A. Effect of couplings

Calculations with coupled channels codes show that the energy dependence of the cross sections above the barrier region is relatively insensitive to the couplings included, and is primarily sensitive to the nuclear potential used. An example, the fusion of $^{16}O$ with the strongly deformed nucleus $^{154}Sm$, is shown in Fig. 1. Note that, in this and similar plots,

the cross sections are shown on a linear scale rather than the usual logarithmic one, where it is difficult to assess the accuracy of fits to data. Calculations were made with the realistic coupled channels code CCFULL [8], which takes coupling, to all orders, uses an ingoing wave boundary condition, and calculates a barrier penetrability for each partial wave. Using the same potential parameters, the results show that there is very little difference, apart from a small reduction in the average barrier energy (≈0.1 MeV), between the fusion cross sections above about 200 mb when there is no coupling (dashed line) and when coupling to the rotational band in $^{154}$Sm is included (full line). For lower cross sections and bombarding energies in the region of the fusion barrier (≈59.3 MeV) there is a major difference between the two calculations since couplings strongly affect the cross sections in this region [2]. Hence, to ensure that the data fitted were above the barrier region, the lowest values of $\sigma_{\rm fus}$ included were at least 200 mb for all reactions.

### B. Fitting procedure

The high energy fusion cross sections were fitted with a $\chi^2$ minimization code based on the simplified coupled channels code CCMOD [7]. The diffuseness determined from fitting a given data set depends somewhat on the other parameters of the WS potential. Thus, in order to carry out a systematic study, a consistent approach is required in fitting the experimental data, as described below. The values of $r_0$ and $a$, together with their uncertainties, giving the best fit to the fusion data, were found for a fixed value of $V_0$. The values of $r_0$ and $a$ are strongly correlated in the sense that a given value for $r_0(a)$ defines, within the error limits, the value for $a(r_0)$ rather precisely. For example, in the case of the $^{16}$O+$^{208}$Pb reaction, fixing $a(r_0)$ at their optimum values defines $r_0(a)$ to about 0.02% (0.06%). Further, an increase in $a(r_0)$ causes a decrease in $r_0(a)$ so that the correct value for $V_B$ is regained. The uncertainties quoted in the fit parameters fully include the effects of this correlation. Generally no couplings were included in the calculations after a few cases were checked to see whether their inclusion made any significant difference to the results; changes were minor (see Sec. II A).

The parent codes of CCMOD, CCFUS and CCDEF, calculate the cross sections using the Wong formula [24]

$$\sigma(E) = (R_B^2 \hbar\omega/2E)\ln\{1+\exp[2\pi(E-V_B)/\hbar\omega]\}. \quad (2)$$

However the Wong formula does not take into account the $l$ dependence of the curvature or barrier radius. It has been shown [25] that neglect of the $l$ dependence of the barrier radius in the energy region $E > V_B$ leads to larger than expected values of $a$. Thus the shift of the barrier to smaller separation distances with increasing $l$ has to be taken into account in order to obtain a meaningful fit to the above-barrier cross sections. One of the features of CCMOD is that, following Ref. [25], this is achieved by replacing $R_B$ in Eq. (2) by

$$R_E = R_B - a\,\ln[1+2(E-V_B)/V_B] \quad (3)$$

for $E > V_B$. The use of the modified Wong formula in CCMOD results in rapid calculations. However, it must be recognized that a result of using this formula is that the loss of the potential pocket at high angular momentum does not limit fusion, unlike in the code CCFULL [8], which solves the Schrödinger equation and uses the ingoing wave boundary condition at the minimum in the pocket. However, until the pocket is lost, CCFULL and CCMOD give essentially identical results for zero-coupling calculations.

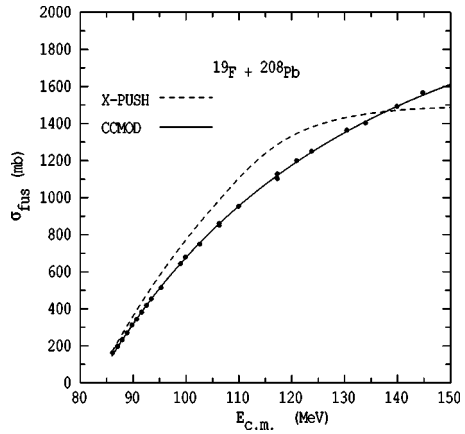


FIG. 2. Experimental excitation function for the reaction $^{19}$F +$^{208}$Pb (filled circles) compared with various calculations. The full line is the fit with CCMOD for $V_0 = 100$ MeV, while the long-dashed line results from a calculation with the extra-push model adjusted to give the experimental value for $V_B$.

The experimental data show no evidence for limitation of fusion due to loss of the potential pocket, being extremely well fitted by CCMOD up to the highest measured energies, for example up to $1.7 \times V_B$ for $^{19}$F+$^{208}$Pb as shown in Fig. 2. This might imply that the pocket does not disappear at the highest $l$ values probed by the data. Alternatively, physical processes not included in coupled channels models such as tangential friction, as for example in the extra-push model due to Swiatecki [26,27], may permit fusion to occur despite the disappearance of the pocket in the entrance-channel potential. However, as discussed later, extra-push model calculations do not reproduce the trend of the data, as seen by the dot-dashed line in Fig. 2. For deeper nuclear potentials the pocket remains up to higher $l$ values. Hence the high energy data can be reproduced by CCFULL, but only with deep nuclear potentials. For such potentials CCMOD and CCFULL agree well. It can be argued that these deep potentials are unrealistic [28,29]. A depth of 100 MeV for $V_0$ is relatively close to the potential depths of the Woods-Saxon parametrization of the exponential Akyüz-Winther potential [12], as described in Ref. [13], which reproduces elastic scattering data. This will later be referred to as the AW potential. Consequently, for this systematic study, the fusion data were fitted with the code CCMOD using a fixed potential depth of 100 MeV. Fixing the depth avoids the dependence of $a$ on $V_0$, which is shown in Fig. 3, together with the dependence of $r_0$, for three experimental systems spanning a wide range of $Z_1Z_2$. As shown in Fig. 3, the parameter $a$ increases and $r_0$ decreases as $V_0$ increases; $\hbar\omega$ increases only slightly with increasing $V_0$ and is not shown.

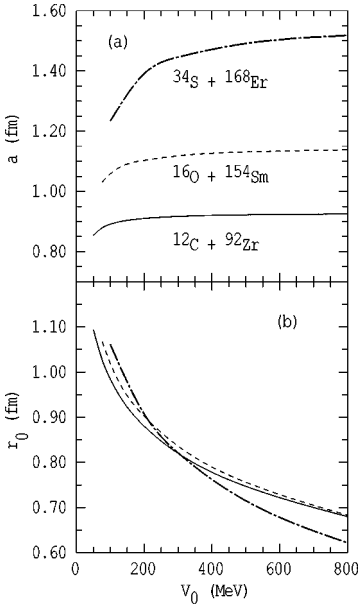


FIG. 3. The values of $a$ and $r_0$ obtained by fitting the high energy cross sections as a function of the potential depth $V_0$ for the systems $^{12}$C+$^{92}$Zr (solid line), $^{16}$O+$^{154}$Sm (dashed line), and $^{34}$S +$^{168}$Er (dot-dashed line).

### C. Total potential

Total potentials (nuclear + Coulomb + centrifugal) $V_T$ for three values of $V_0$, as functions of the center of mass separation distance $r$, are shown in Figs. 4 and 5 for systems with low and high values of $Z_1Z_2$, respectively. Potential parameters giving the same barrier energy for different depths were obtained by the following method. High energy cross sections were generated by CCFULL or CCMOD using the AW potential. Results from the two codes agreed except for a few

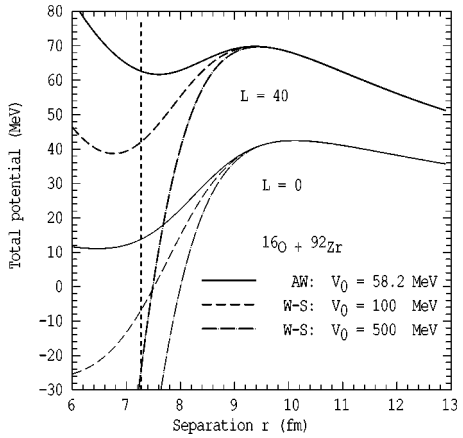


FIG. 4. Total potentials $V_T$ for the reaction $^{16}$O+$^{92}$Zr. Potentials for angular momenta of $0\hbar$ and $40\hbar$ are shown using the nuclear potential of Akyüz and Winther having $V_0$=58.2 MeV (full lines) and potentials with $V_0$=100 (dashed line) and 500 MeV (dot-dashed line), which reproduce the same above-barrier fusion cross sections. The vertical dotted line gives an indication of the separation distance when the overlap nuclear density reaches the saturation density.

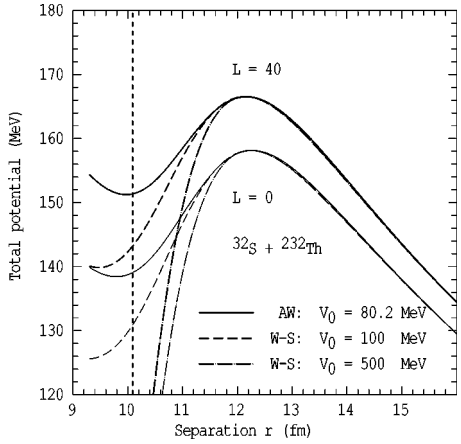


FIG. 5. Total potentials $V_T$ for the reaction $^{32}$S+$^{232}$Th. Potentials for angular momenta of $0\hbar$ and $40\hbar$ are shown using the nuclear potential of Akyüz and Winther having $V_0$=80.2 MeV (full lines) and potentials with $V_0$=100 (dashed lines) and 500 MeV (dot-dashed lines), which reproduce the same above-barrier fusion cross sections. The vertical dotted line gives an indication of the separation distance when the overlap nuclear density reaches the saturation density.

cases with very large $Z_1Z_2$, when the potential depth was too small for CCFULL. The fitting code was then used to reproduce these cross sections for the fixed depths of 100 and 500 MeV by optimizing the values of $a$ and $r_0$. Potentials for angular momenta $0\hbar$ and $40\hbar$ are illustrated. At and outside the barriers, the $V_T$ for different $V_0$ are essentially identical but, at smaller separations, they differ increasingly. Higher angular momenta also probe the region inside the $l$=0 barrier; thus the excitation function above the barrier is also sensitive to $V_0$. That is why, in this systematic study, a fixed value of 100 MeV was used. The potential with $V_0$ =100 MeV, having slightly different values of $a$ and $r_0$ from the AW values, will later be referred to as the modified Akyüz-Winther potential (MAW).

The vertical dotted lines in Figs. 4 and 5 show the separations corresponding approximately to those of the sum of the half-density radii $R_{1/2}$ of targets and projectiles. Values for $R_{1/2}$ have been estimated from the compilation of de Vries *et al.* [30]. The potentials clearly have no meaning for separations smaller than these as the summed nuclear densities are then greater than the saturation density $\rho_0$. For such separations it is clearly necessary to incorporate additional shape degrees of freedom into the calculations. Taking the diffuseness parameter of the density distribution as 0.56 fm [30], the summed density for separations 1 fm and 2 fm larger than those of the dotted lines would be about $0.58\rho_0$ and $0.29\rho_0$, respectively. The frozen density approximation may be suspect even for these separations. Therefore it can be seen from Figs. 4 and 5 that the main differences, which have significance for fusion, between the $V_T$ for differing values of $V_0$ occur in the regions of $r$ just inside the fusion barrier. Notably the potential minima occur in the regions of $r$ where the potentials are meaningless. The barriers are similar for all $V_0$ but inside the barrier radius the total potential drops more quickly with increasing $V_0$. This can have a large effect on the sub-barrier cross sections because the barriers

become thinner as $V_0$ increases. The penetrabilities correspondingly increase significantly with $V_0$ for bombarding energies well below the barrier, resulting in larger values of $\sigma_{\rm fus}$.

### D. Accuracy of measured cross sections

The data used in this survey were taken from measurements aimed at determining barrier distributions. These required much higher precision than had previously been the case for measurements of $\sigma_{\rm fus}$. Two aspects are of especial importance. The values of $\sigma_{\rm fus}$ need to be determined with a *relative* accuracy of about ±1% or at worst a few percent. However, the absolute accuracy of the cross sections is not of great importance for the purpose of determining a barrier distribution. The measurements have to be taken with closely spaced center of mass energy intervals (≈1 MeV), which should also be very well defined to ≈20 keV or better. In some cases it is clear that the stated errors are too small, giving fits with values of $\chi^2$ per degree of freedom ($\chi^2/\nu$) significantly exceeding unity. Whether these result from larger errors in the cross sections or in the energy intervals cannot be determined. In the cases where $\chi^2/\nu$ exceeded 1.5 the uncertainties on $a$ and $r_0$ were multiplied by $(\chi^2/\nu)^{0.5}$ (this is equivalent to multiplying the stated uncertainties in $\sigma_{\rm fus}$ by the same quantity). In a few cases, isolated points were omitted from the experimental excitation function when they were clearly out of line (>3 standard deviations) with the trend of the data.

Some measurements yield accurate values for the absolute fusion cross sections (see, for example, Ref. [31]). However, for others, such as those using electrostatic deflectors [32], it is more difficult to determine absolute cross sections, although the relative cross sections may be well determined. This is because the transmission of the deflectors can be significantly less than unity and may be difficult to determine accurately. If the absolute value of $\sigma_{\rm fus}$ is in error, but is assumed to be correct, the deduced values of the parameters $a$, $r_0$, $R_B$, and $\hbar\omega$ can be seriously in error. An "efficiency factor" $\epsilon$ was therefore introduced in the code in order to account for possible errors in the absolute cross sections. For example, $\epsilon=1.0$ would mean that we assume the absolute cross sections to be correct, whereas $\epsilon=0.8$ would mean that they were taken to be 20% too low.

As shown in Ref. [25] the barrier radius decreases strongly with increasing angular momentum for large values of $a$, whereas it is almost constant for small $a$. Thus the calculated fusion cross sections at above-barrier energies are progressively reduced as $a$ increases. A measurement which is assumed to be 100% efficient but actually has a lower efficiency may therefore incorrectly suggest a value of $a$ which is too large. An example of how $a$ and $r_0$ vary with $\epsilon$ is shown in Fig. 6, for the $^{16}$O+$^{208}$Pb reaction, where it is seen that a ±10% change in $\epsilon$ results in about a ±25% change in $a$ for $a=1.11$ fm. The corresponding changes in $r_0$, $R_B$, and $\hbar\omega$ are about ±7%, ±4%, and ±18%, respectively, whereas $V_B$ remains almost unaltered. Unfortunately these changes also depend on the value of $a$. For the ±10% change in $\epsilon$, the changes in $a$ and $r_0$ are about ±30% and ±9% if

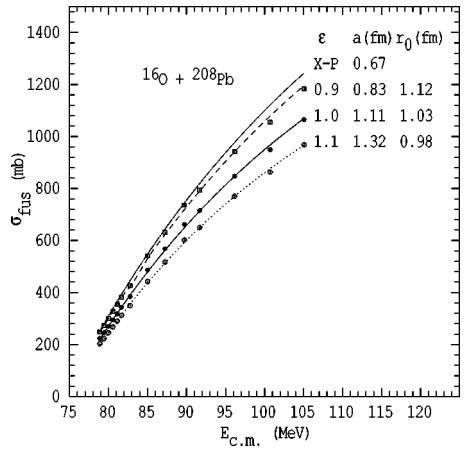


FIG. 6. Excitation functions for the reaction $^{16}$O+$^{208}$Pb, assuming $\epsilon$ has the values 0.9, 1.0, and 1.1. The experimental points are indicated by filled circles [11]. The open points represent the latter divided by the indicated values of $\epsilon$; the corresponding values of $a$ and $r_0$ required to fit these data with $V_0=100$ MeV are also shown. The dashed and dotted lines are the fits to the points giving the values of $a$ and $r_0$ shown. The dot-dashed line, labeled X-P, derives from a calculation with the extra-push model adjusted to give the experimental $V_B$.

$a=0.9$, but are ±8% and ±2%, respectively, for $a=1.4$ fm. Even those experiments which claim a high degree of accuracy in absolute cross section might be expected to have a systematic uncertainty of perhaps ±2%, corresponding to a range of $a$ between ±6% and ±2% depending on the value of $a$, whereas others (see, for example, Ref. [33]) are stated to have an uncertainty in cross section normalization of as much as ±15%. Thus it is expected that values determined from fitting experimental data will show considerable scatter.

In making a useful systematic study of the experimental values of $a$, it is clearly neccessary to be able to identify inaccuracies in measurements of absolute cross sections to estimate the values of $\epsilon$. One possible way is to systematically compare experimental values of $r_0$ with values derived from a theoretical potential, such as that of Akyüz and Winther [12,13] or the more recent semimicroscopic potential of Denisov [34]. It would not be reasonable to expect exact correspondence between the experimental and theoretical values. However, a smooth trend in the differences or ratios might be expected, if plotted against the charge product $Z_1Z_2$. Any large departures from this trend would indicate an error in absolute cross section. The parameter $\epsilon$ could then be adjusted to bring $r_0$ in accordance with the trend values. In 10 systems out of 46 there was a need to change $\epsilon$ from unity. Values of $\epsilon$ cannot be determined with precision by this method, and hence realistic errors for the $a$ values are almost certainly larger than those derived from $\chi^2$ fits to the high energy cross sections.

## III. RESULTS AND COMPARISON WITH THEORETICAL BARE POTENTIALS

### A. Bare potentials

In principle, a coupled channels calculation should start with a "bare" nuclear potential, i.e., one calculated from

nuclear density distributions and appropriate interactions between the nucleons. Such a potential by definition does not include the effects of any couplings. Using such a potential, all strongly coupled, mainly collective, channels should be included in coupled channels calculations. Coupling to states with excitation energies $E_x \leqslant \hbar\omega$ (typically 2–4 MeV) mainly produce a change in the shape of the barrier distribution. On the other hand, coupling to states with $E_x > \hbar\omega$ results mainly in potential renormalization, shifting down the value of $V_B$ relative to that obtained using the bare potential [35,36].

The best known example of this potential shift relates to the case of coupling to the collective $3_1^-$ state of $^{16}$O at $E_x = 6.05$ MeV. This produces a downward shift of about 2 MeV in $V_B$ for the case of $^{16}O + ^{144}Sm$ [35]. The shift can qualitatively be understood by the short vibrational period associated with coupling to this state, meaning that it can respond quickly (adiabatically) to the forces acting upon it, which has the effect of reducing $V_B$. In contrast, the period of rotation of a heavy statically deformed nucleus is so long that no significant change in orientation can occur during the collision time. When, as in this work, the nuclear potential has been determined by fitting high energy fusion data, the result is not a bare potential, but rather an effective potential. This is because couplings to states at high excitation energy, which cause barrier shifts, have not been included in the calculations. Thus for fusion reactions with $^{16}$O, the effects of the $3_1^-$ state in $^{16}$O would be implicitly included in the effective potential and hence coupling to this state should not be explicitly included in a coupled channels calculation. It also follows from this discussion that a realistic bare potential, without couplings, should give a value for $V_B$ exceeding the experimental value. This does not seem to be the case with double-folding potentials calculated using density-dependent M3Y effective nucleon-nucleon interactions [16]. If radial dissipation played a part in the fusion process, the measured value for $V_B$ would be increased over that calculated without friction. However, if this were the case it would mean that collisions would be occuring between the surface nucleons, which might invalidate the frozen density assumption.

The AW potential [13] has sometimes been taken as a bare potential [36]. However, though partly based on the proximity potential, it derives from a least-squares fit to experimental elastic scattering data, and therefore may not be the best choice for the description of fusion data.

The recent potential of Denisov [34], based on a semimicroscopic calculation, might be regarded as a better approximation to a bare potential. These potentials were calculated for projectile and target nuclei between $^{16}$O and $^{212}$Po in the extended Thomas-Fermi approximation and assuming frozen densities. An analytical expression was then derived by fitting calculated potentials for 7140 reactions and was claimed to reproduce the barrier heights calculated semimicroscopically with a rms error less than 0.3 MeV [34]. This expression may, however, be much more inaccurate outside the calculated range of nuclei. In order to see whether this might be so, the values of $V_B$ derived from the analytical expression and those calculated from the AW potential were compared. Although not identical, one would expect a

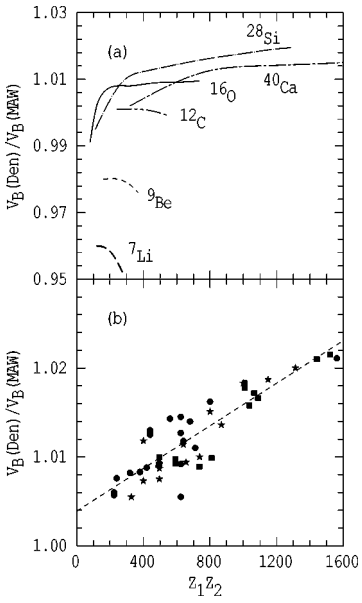


FIG. 7. (a) Ratio between the fusion barriers calculated from the analytical formula of Denisov [$V_B$(Den)] and from the AW potential [$V_B$(AW)] for the following projectiles: $^{7}$Li (dotted line); $^{9}$Be (dashed line); $^{12}$C(dash-dot-dotted-line); $^{16}$O (solid line); $^{28}$Si (long-dash-dotted-line); $^{40}$Ca (long-dash-short-dashed-line). (b) Corrected ratios of the barriers for the two potentials (see text). The symbols indicate target nuclei with closed shells (stars), of vibrational character (circles), and of rotational character (squares). This convention is used in later figures.

smooth trend in the ratio of the two results, which are shown in Fig. 7(a) for a number of different projectiles, against $Z_1Z_2$. While the ratios for $^{16}$O and higher mass projectiles lie within a range of about ±0.1% there is a sudden drop in the ratios for projectiles lighter than $^{16}$O. The Denisov barriers for $^{12}$C and $^{9}$Be have therefore been corrected by increasing them so that the values of $V_B$(Den)/$V_B$(AW) follow the trend of the $^{16}$O ratios. After correction, the ratios calculated for all the systems used for this study are shown in Fig. 7(b), together with a linear fit to the points (dashed line). The results scatter about this line with a full width at half maximum of about 0.2%.

### B. Comparison with measured fusion barriers

In Fig. 8 the differences $\delta V_B$ between the values of $V_B$ from Denisov and those obtained from fits to the high energy cross sections are shown as a function of $Z_1Z_2$. Each error shown is derived by taking the square root of the quoted uncertainty in beam energy and an arbitrary 20% of the energy loss in the target added in quadrature. An additional uncertainty in $V_B$, not included, arises from the statistical errors in the data. It can vary from about ±0.02 MeV to about ±0.3 MeV for the worst cases such as $^{18}O + ^{198}Pt$. Mostly they are comparable to or smaller than the errors shown in the figure. The values of $\delta V_B$ are positive, as expected, and generally increase with increasing $Z_1Z_2$. The dashed line is a linear least-squares fit to the data. If the Denisov potential were a true bare potential and if the $\delta V_B$

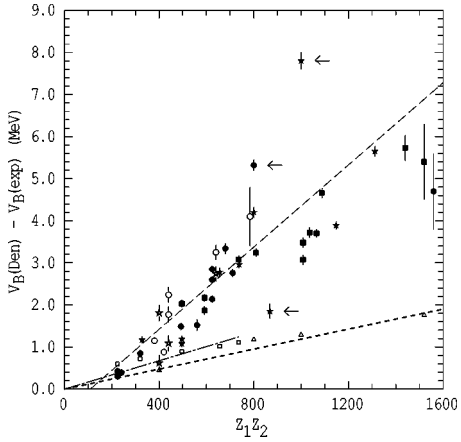


FIG. 8. Difference between the Coulomb barriers calculated with the Denisov potential and the experimental barriers. The Denisov result has been corrected for $^{9}$Be and $^{12}$C projectiles (see text). The dashed line is a linear least-squares fit to the experimental data. The dash-dotted line and the dotted line show the trends (assumed linear) of calculations, with the code CCFULL, including the isoscalar GQR for reactions induced by $^{16}$O and $^{40}$Ca, respectively. Some calculated points are shown for $^{16}$O (small open squares) and for $^{40}$Ca (small open triangles). The horizontal arrows point to the three extreme cases of $^{40}$Ca+$^{96}$Zr and $^{124}$Sn (high) and $^{28}$Si+$^{144}$Sm (low). Symbols are as in Fig. 7, except that the open symbols indicate cases where $\epsilon \neq 1.0$.

could be correctly described by coupling to highly excited states using a real potential (e.g., without friction), then it would be expected that the dashed line would go through zero for $Z_1Z_2=0$. However, neither of these assumptions may be correct, in which case there is no reason why it should do so. Most of the data lie fairly close to the line; however, there are some exceptions, The most notable are $^{29}$Si $+^{144}$Sm ($Z_1Z_2=868$), which lies about 2 MeV below the line, $^{40}$Ca+$^{124}$Sn ($Z_1Z_2=1000$), $\approx$3 MeV above, and $^{40}$Ca+$^{96}$Zr ($Z_1Z_2=800$), $\approx$2 MeV above. Possible reasons for these) large deviations will be discussed later. However, they cannot be due to uncertainty in $\epsilon$ since this has a minor effect on $V_B$. For example, even a 20% change in $\epsilon$ would produce an approximately 0.3 MeV change in $V_B$, which is comparable with the uncertainties shown in Fig. 8. An effect that might cause scatter about the line is the variation of the excitation energies of $3_1^-$ states, which can be above or below the values of $\hbar\omega$. Unlike the collective first $2^+$ states, whose energies generally lie well below $\hbar\omega$ and whose $B(E2)$ values decrease rather systematically with increasing excitation energy [37], there is no clear relationship between excitation energy and $B(E3)$ for the $3_1^-$ states. Their strengths, expressed as a percentage of the energy weighted sum rule, vary from about 0.4% to 16% [38]. Thus states with large $B(E3)$ values, such as the $3_1^-$ state of $^{16}$O, may exist at energies above $\hbar\omega$ and produce large barrier shifts, whereas states with similar $B(E3)$ at energies below $\hbar\omega$ would produce smaller shifts. Since the low energy octupole strength is known often to be fragmented among a number of $3^-$ states it might be more appropriate to consider all of this strength rather than just that in the $3_1^-$ state. Metlay *et al.* [39] have plotted these measured total strengths as a function of the centroid energy.

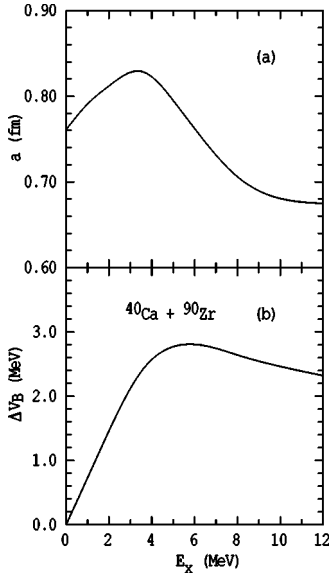


FIG. 9. Calculations showing the variation of (a) the fitted diffuseness parameter $a$ and (b) the barrier shift $\Delta V_B$ as a function of the assumed excitation energy of the $3_1^-$ state in $^{40}$Ca, for the reaction $^{40}$Ca+$^{90}$Zr (see text).

Although there is weak evidence for systematic behavior, there is very large scatter in the data.

Excited states with $E_x > \hbar\omega$ not only produce a reduction $\Delta V_B$ in $V_B$ but also have some effect on the parameters $a$ and $r_0$. This is illustrated in Fig. 9 for the barrier shift $\Delta V_B$ and the parameter $a$ in the case of $^{40}$Ca+$^{90}$Zr. We used the realistic coupled channels code CCFULL [8], including only the $3^-$ state of $^{40}$Ca, with $\beta_3=0.433$ [38]. In order to generate hypothetical "data" for fusion cross sections for this system, the energy of the $3_1^-$ state of $^{40}$Ca was allowed to vary from the experimental value of 3.74 MeV. The barrier parameters were then extracted in the same way as for experimental data. In these calculations the AW potential [12,13], modified to $V_0=400$ MeV (see Sec. II C), was used. This was done because coupled channels calculations with CCFULL [8] require deep potentials to reproduce the fusion cross sections over the entire energy range. Although the changes in $a$ are significant, they are generally small ($\approx \pm 0.08$ fm) compared to the deviations between the values obtained from fits to high energy fusion data and those from the MAW potential, which on the average are about 0.4 fm (see Fig. 12 below).

### C. Effect of giant resonances

A general feature of nuclei is that they have collective giant resonances (GR) at high excitation energies [40,41]. Coupling to these produces a barrier shift, which would be expected to increase with the coupling strength $Z_1Z_2$. The GR with multipolarity $\lambda$ of 0, 1, and 2 are well known, whereas those with higher $\lambda$ may well exist but are difficult to identify experimentally. To give some feeling for the effect of coupling to these GR, calculations have been made for the isoscalar $E2$ resonance (GQR) alone. This is known to be centered at an energy of about $65A^{-1/3}$ MeV. The GR deformation parameter $\beta_\lambda$ for $\lambda \geqslant 2$ is given by [40]

$$\beta_\lambda^2 \simeq \frac{2\pi\hbar^2\lambda(2\lambda+1)}{3mAR^2E_x}, \tag{4}$$

where $m$ is the nucleon mass and $R$ the nuclear half-density radius. For $\lambda=2$ and $R=1.2A^{1/3}$ fm, $\beta_2=3.04A^{-2/3}$, giving a variation in $\beta_2$ from the rather small value of 0.087 for $^{208}$Pb to 0.58 for $^{12}$C. The realistic all-order coupled channels code CCFULL [8] has been used to estimate the barrier shifts due to the GQR, $\beta_2$ values for both target and projectile being included. The finite width [42] of the GQR was not taken into account as the effects are not expected to be significant. Also shown in Fig. 8 are some of the calculated points for $^{16}$O and $^{40}$Ca projectiles. Approximate linear trend lines, forced to go through zero, are also shown for $^{16}$O projectiles (long-dash-dotted line) and $^{40}$Ca projectiles (dotted line). Both exhibit similar behavior although they differ in magnitude. The reason why the $^{16}$O results lie above those for $^{40}$Ca is because the values for $\beta_2$ increase strongly as $A$ decreases, making the effect of the projectile dominant in most cases. However, the effect of the target nucleus becomes relatively more important as the target mass ($Z_1Z_2$) decreases.

The calculated shifts explain up to about 1/3 of the experimental deviations and show a similar dependence on $Z_1Z_2$ as the data, suggesting that coupling to all giant resonances may account for a significant part of the trend in the experimental data shown in Fig. 8.

### D. Radius parameters

The calculations to determine the parameters $a$ and $r_0$ giving the best fit to experimental data were initially carried out assuming that the absolute cross sections were correct, i.e., taking $\epsilon=1$. The comparisons of the experimental values of $r_0$ have been done only with values from the modified Akyüz-Winther potential [13], since Denisov's parametrization is not of the Woods-Saxon form and thus does not involve $r_0$. Values of $r_0$(MAW) and $a$(MAW) for the MAW potential (see Sec. II C) were determined for a number of reactions and interpolated to obtain values for $r_0$(MAW) for the other cases. The ratios $r_0$(expt)/$r_0$(MAW) are shown in Fig. 10, plotted against $Z_1Z_2$. Some typical uncertainties in the ratios, arising from statistical uncertainties in the data, are indicated. A 2% uncertainty in $\epsilon$ would result in a further uncertainty of about 0.013 in the ratio, which is comparable with the statistical errors.

The results of the analysis of the high energy cross sections indicate that the values of $r_0$(expt)/$r_0$(MAW) are consistent with a value of $0.932\pm0.021$. There is a slight tendency for the closed-shell target nuclei to have higher values of $r_0$(expt)/$r_0$(MAW). Values for closed-shell, vibrational, and deformed nuclei are $0.941\pm0.020$, $0.928\pm0.020$, and $0.930\pm0.024$, respectively, but the effect is not significant.

In a number of cases, the values of $r_0$(expt)/$r_0$(MAW) for $\epsilon=1$ were far outside the scatter range of Fig. 10. For each of these $\epsilon$ was changed from unity so that $r_0$(expt)/$r_0$(MAW) assumed the average value of $0.932\pm0.021$ (see Table I). These cases are not shown in Fig. 10. The reactions $^{36}$S $+^{90,96}$Zr [33] are an example, implying that in this case $\sigma_{\rm fus}$ had been overestimated by a substantial amount. For all of the cases where $\epsilon=1$, the experimental cross sections lie below a fusion excitation function calculated with the AW potential, for which $r_0$ has been slightly adjusted to give the same fusion barrier as that determined experimentally; this implies that $a$(expt)$>a$(MAW). The opposite is the case for $^{36}$S$+^{90,96}$Zr reactions, shown in Fig. 11 for the $^{90}$Zr case, implying that $a$(MAW)$>a$(expt), in strong disagreement with most other data.

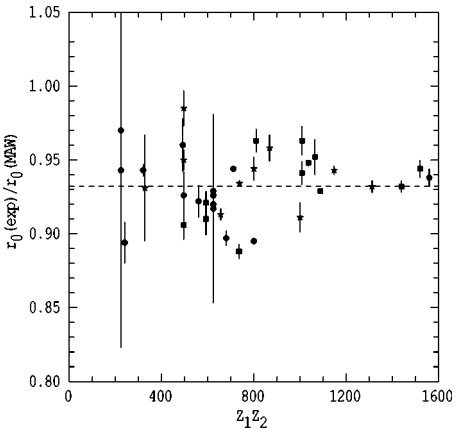


FIG. 10. Values of $r_0$(expt)/$r_0$(MAW) as a function of $Z_1Z_2$ (see text). A few typical uncertainties are indicated. The dashed line shows the average value of the ratio for all cases where $\epsilon$ has been taken to be unity. Cases where $\epsilon$ appeared to deviate markedly from unity are not included. Symbols are as in Fig. 7.

### E. Diffuseness parameters

The values of the parameters $a$, $r_0$, $V_B$, $R_B$, and $\chi^2$ per degree of freedom ($\chi^2/\nu$) deduced from fitting the experimental data, as described in Sec. II, are shown in Table I. Uncertainties in values of the fitting parameters $a$ and $r_0$ are shown. However, we have not included uncertainies for $V_B$ and $R_B$ because we do not wish to give undue physical significance to these values, as they depend on the validity of the barrier passing model which is used. If fusion cross sections were reduced by deep-inelastic collisions the fitted value of $R_B$ would be too small and $V_B$ would also be in error if the ratio of fusion to deep-inelastic cross sections was not independent of bombarding energy. In order to give some indication of the quality of the data, the table also shows the average quoted percentage experimental errors, multiplied by $(\chi^2/\nu)^{0.5}$ when $\chi^2/\nu \geq 1.5$. This quantity is a measure of the average deviation of the data from the best fit. More than half have an average deviation of less than 1.5%, showing that the fits represent the experimental results extremely well. Values deduced for $\epsilon\neq1$ are indicated in the table. For the $^{9}$Be$+^{208}$Pb case, the weakly bound projectile $^{9}$Be breaks up before fusion occurs [43,44], so that fusion is inhibited. Therefore for this reaction the measured incomplete fusion cross sections were added to the complete fusion cross sections and the sums fitted to obtain the potential parameters.

Values of $a$, for $V_0=100$ MeV, are shown as a function of $Z_1Z_2$ in Fig. 12(a). The experimental errors shown arise from statistical errors in the data together with, in some cases,

TABLE I. Parameters $a$ and $r_0$ for the real nuclear potential determined by fitting the high energy fusion cross sections with $V_0$ fixed at 100 MeV. The uncertainties, shown in parenthesis, are the products of those determined from the fits and $(\chi^2/\nu)^{0.5}$ (see text). Fusion barriers $V_B$, fusion radii $R_B$, values of $\chi^2$ per deg of freedom $(\chi^2/\nu)$, and products of the average quoted percentage errors of the data and $(\chi^2/\nu)^{0.5}$ ($\Delta$) are also given. Cases where the values were derived from nonunity values for $\epsilon$ are indicated.

| Reaction | $a$ (fm) | $r_0$ (fm) | $V_B$ (MeV) | $R_B$ (fm) | $\chi^2/\nu$ | $\Delta$% | Reference |
|---|---|---|---|---|---|---|---|
| $^{16}$O+$^{58}$Ni | 0.78(3) | 1.031(10) | 31.67 | 9.30 | 1.8 | 1.0 | [65] |
| $^{16}$O+$^{62}$Ni | 0.74(4) | 1.063(8) | 31.12 | 9.54 | 2.8 | 1.2 | [65] |
| $^{12}$C+$^{92}$Zr | 0.89(3) | 0.984(15) | 32.31 | 9.68 | 0.5 | 0.9 | [54] |
| $^{16}$O+$^{92}$Zr | 0.841(11) | 1.046(4) | 41.96 | 10.02 | 1.5 | 0.9 | [54] |
| $^{9}$Be+$^{208}$Pb | 0.903(10) | 1.04(4) | 38.19 | 11.35 | 0.4 | 3.1 | [43] |
| $^{16}$O+$^{112}$Sn | 0.88(6) | 1.05(3) | 51.02 | 10.2 | 2.6 | 1.5 | [66][a] |
| $^{16}$O+$^{116}$Sn | 0.86(6) | 1.05(3) | 50.96 | 10.29 | 4 | 1.7 | [66][b] |
| $^{40}$Ca+$^{48}$Ca | 0.93(9) | 1.05(3) | 52.00 | 9.99 | 13 | 4.3 | [51][c] |
| $^{48}$Ca+$^{48}$Ca | 0.89(10) | 1.04(3) | 51.49 | 10.16 | 42 | 6.7 | [51][d] |
| $^{40}$Ca+$^{46}$Ti | 0.97(6) | 1.04(2) | 57.89 | 9.77 | 3 | 2.0 | [67][e] |
| $^{40}$Ca+$^{48}$Ti | 0.95(6) | 1.04(2) | 57.88 | 9.85 | 5.1 | 2.7 | [67][f] |
| $^{40}$Ca+$^{50}$Ti | 0.89(6) | 1.04(2) | 58.21 | 9.84 | 4.3 | 2.5 | [67][g] |
| $^{12}$C+$^{204}$Pb | 0.85(7) | 1.08(2) | 57.55 | 11.34 | 3.5 | 3.4 | [68] |
| $^{16}$O+$^{144}$Sm | 0.75(4) | 1.108(13) | 61.03 | 10.85 | 6.3 | 1.7 | [2] |
| $^{16}$O+$^{148}$Sm | 0.99(6) | 1.04(2) | 59.83 | 10.76 | 3.9 | 2.0 | [2] |
| $^{16}$O+$^{154}$Sm | 1.06(2) | 1.019(7) | 59.35 | 10.76 | 0.8 | 1.0 | [2] |
| $^{17}$O+$^{144}$Sm | 0.87(2) | 1.069(8) | 60.57 | 10.79 | 3.3 | 1.1 | [2] |
| $^{28}$Si+$^{92}$Zr | 0.97(4) | 1.040(13) | 70.93 | 10.19 | 1.8 | 1.3 | [54] |
| $^{16}$O+$^{182}$W | 1.06(5) | 1.027(13) | 69.49 | 10.98 | 0.45 | 2.7 | [69] |
| $^{16}$O+$^{186}$W | 1.04(4) | 1.039(10) | 68.87 | 11.12 | 1.8 | 1.4 | [2] |
| $^{32}$S+$^{89}$Y | 1.01(4) | 1.050(9) | 77.77 | 10.30 | 0.52 | 1.0 | [70] |
| $^{34}$S+$^{89}$Y | 1.04(3) | 1.047(8) | 76.88 | 10.40 | 0.94 | 1.0 | [70] |
| $^{16}$O+$^{194}$Pt | 1.09(14) | 1.04(4) | 71.54 | 11.23 | 0.3 | 6.0 | [71] |
| $^{18}$O+$^{198}$Pt | 1.1(2) | 1.04(6) | 70.79 | 11.38 | 6.1 | 9.9 | [71] |
| $^{36}$S+$^{90}$Zr | 0.97(9) | 1.07(3) | 77.97 | 10.54 | 0.86 | 1.6 | [33][h] |
| $^{36}$S+$^{96}$Zr | 1.21(8) | 1.03(3) | 75.61 | 10.79 | 1.9 | 2.1 | [33][h] |
| $^{16}$O+$^{208}$Pb | 1.11(2) | 1.035(5) | 74.52 | 11.31 | 5.1 | 1.2 | [11] |
| $^{35}$Cl+$^{92}$Zr | 1.21(3) | 1.016(6) | 82.94 | 10.20 | 2.8 | 1.1 | [54] |
| $^{19}$F+$^{197}$Au | 1.005(12) | 1.069(3) | 81.61 | 11.32 | 1.1 | 0.8 | [68] |
| $^{16}$O+$^{238}$U | 1.28(3) | 1.007(6) | 80.81 | 11.45 | 3.5 | 1.0 | [68] |
| $^{19}$F+$^{208}$Pb | 1.062(7) | 1.059(2) | 82.96 | 11.50 | 2.2 | 0.7 | [72] |
| $^{58}$Ni+$^{60}$Ni | 1.12(14) | 1.06(3) | 96.00 | 10.26 | 0.8 | 2.7 | [73][i] |
| $^{40}$Ca+$^{90}$Zr | 1.05(4) | 1.073(8) | 96.88 | 10.53 | 0.9 | 0.9 | [45] |
| $^{40}$Ca+$^{96}$Zr | 1.383(15) | 1.017(2) | 94.59 | 10.12 | 0.2 | 0.9 | [45] |
| $^{19}$F+$^{232}$Th | 0.96(4) | 1.094(9) | 89.30 | 11.91 | 0.5 | 1.0 | [74] |
| $^{28}$Si+$^{144}$Sm | 0.89(4) | 1.089(10) | 103.89 | 10.93 | 1.1 | 1.1 | [46] |
| $^{40}$Ca+$^{124}$Sn | 1.57(8) | 1.040(9) | 112.93 | 10.08 | 1.4 | 1.5 | [32] |
| $^{28}$Si+$^{178}$Hf | 1.06(4) | 1.075(9) | 115.27 | 11.21 | 5.9 | 1.8 | [75] |
| $^{29}$Si+$^{178}$Hf | 0.94(5) | 1.099(11) | 115.06 | 11.44 | 0.8 | 1.5 | [75] |
| $^{30}$Si+$^{186}$W | 1.053(12) | 1.083(2) | 116.23 | 11.47 | 0.8 | 0.8 | [68] |
| $^{31}$P+$^{175}$Lu | 1.02(8) | 1.088(9) | 120.99 | 11.34 | 5.0 | 2.5 | [75] |
| $^{34}$S+$^{168}$Er | 1.234(12) | 1.061(2) | 122.39 | 11.01 | 1.4 | 1.0 | [76] |
| $^{28}$Si+$^{208}$Pb | 1.08(2) | 1.080(3) | 128.07 | 11.45 | 1.5 | 1.2 | [10] |
| $^{32}$S+$^{208}$Pb | 1.30(3) | 1.072(4) | 144.03 | 10.91 | 3.9 | 1.1 | [77] |
| $^{32}$S+$^{232}$Th | 1.39(6) | 1.071(4) | 155.73 | 11.18 | 0.8 | 1.0 | [77] |
| $^{40}$Ca+$^{192}$Os | 1.18(3) | 1.094(6) | 168.07 | 11.05 | 2.5 | 0.5 | [78] |
| $^{40}$Ca+$^{194}$Pt | 1.26(13) | 1.087(6) | 172.87 | 11.05 | 11 | 1.7 | [78] |

[a] $\epsilon$=1.08.
[b] $\epsilon$=1.10.
[c] $\epsilon$=1.40.
[d] $\epsilon$=1.32.
[e] $\epsilon$=1.07.
[f] $\epsilon$=1.06.
[g] $\epsilon$=1.04.
[h] $\epsilon$=1.25.
[i] $\epsilon$=0.61.

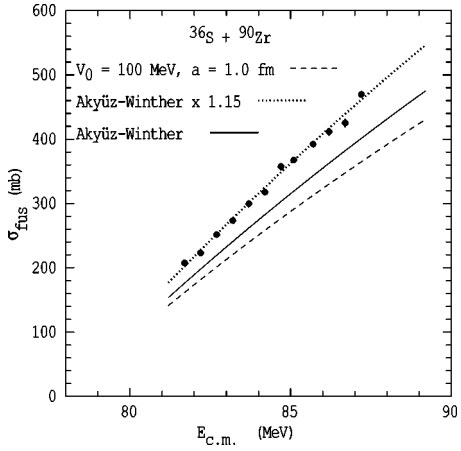


FIG. 11. Comparison of fusion excitation function calculated with the MAW potential, slightly adjusted to give the experimental value of $V_B$ (solid line) with experimental data for the $^{36}S+^{90}Zr$ reaction [33] (see text). The dotted line shows these calculations multiplied by 1.15, indicating the ambiguity between $\epsilon$ and the value of $a$. For comparison the dashed line shows a calculation for $V_0=100$ MeV with $a=1.0$ (typical for other reactions) adjusted to give the experimental $V_B$.

errors arising when $\epsilon$ is not unity. The trend in the data is illustrated by the dashed line, which is a linear least-squares fit to the data, while the full line indicates the values of $a$ for the MAW potential. The points show considerable scatter about the dashed line but are well above those for the MAW potential. Using values of $a$ taken from the dashed line in Fig. 12(a), a 2% change in $\epsilon$ would result in changes in $a$ of approximately 0.06 fm for the systems with low $Z_1Z_2$ down to 0.02 fm for those with high $Z_1Z_2$. Thus errors arising from uncertainties in $\epsilon$ can sometimes be significantly larger than the statistical errors.

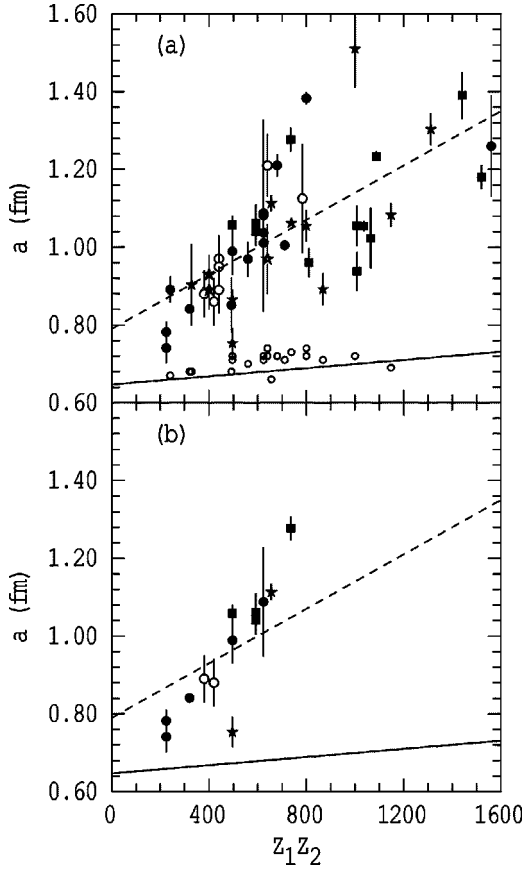


FIG. 12. Values of the diffuseness parameter $a$ as a function of $Z_1Z_2$: (a) for all cases; (b) for $^{16}O$ induced reactions only. The dashed lines show a linear least-squares fit to all of the experimental data and the solid lines indicate the values of $a$ for the MAW potential. Symbols are as in Figs. 7 and 8, except that the small open circles indicate values calculated with the double-folding model [16].

## IV. DISCUSSION OF DIFFUSENESS PARAMETER

The values of $a$ increase on the average with increasing $Z_1Z_2$ and greatly exceed those given by the MAW or AW potential [13]. However, there are considerable fluctuations about the dashed line in Fig. 12(a). The reasons for the large values of $a$ and for the fluctuations are still not clear. In some cases the fluctuations may arise from departures in $\epsilon$ from unity, a value assumed in most cases. To avoid confusion from different projectile structure it is of interest to look at data from a single projectile. Values of $a$ for reactions induced by $^{16}O$, the projectile with the largest number of reactions measured, are shown in Fig. 12(b); the dashed and full lines from Fig. 12(a) are also included. These data, as a function of $Z_1Z_2$, appear to have a steeper slope than that of the dashed line. However, it might be unwise to conclude that different projectiles give different slopes because of this small data set and the large fluctuations about the trend line seen in Fig. 12(a). Many of these cases, including the reactions on $^{144,148,154}Sm$, were measured by the same group [2] and with a compact velocity filter [31] having $\epsilon\approx1.0$. Comparisons between them should therefore be more reliable than comparisons between members of the whole data set.

### A. Effects of neutron number on the diffuseness

To try to get some more understanding of the phenomena driving these results it is worth while to consider some of the reactions, measured by the same groups, which show systematic behavior or show exceptionally large deviations from the dashed line in Fig. 12. Examples of the former are $^{16}O+^{144,148,154}Sm$ and $^{17}O+^{144}Sm$ [2] ($Z_1Z_2=496$) and $^{36}S,^{40}Ca+^{90,96}Zr$ [33,45] ($Z_1Z_2=640$ and 800, respectively). The $^{16}O+^{A}Sm$ reactions show a steady decrease both in $V_B$, relative to Denisov's value, and in $r_0(\text{expt})/r_0(\text{AW})$, and a steady increase in $a$ going from $^{144}Sm$ to $^{154}Sm$; use of $^{17}O$ as a projectile shows similar behavior to increasing mass for the Sm isotopes (see Figs. 8, 10, and 12, and Table I). The $^{36}S$ and $^{40}Ca$ induced reactions on $^{90,96}Zr$ also show similar behavior in going from $^{90}Zr$ to $^{96}Zr$. While the Sm isotopes show a systematic increase in $\beta_2$ going from the spherical

closed shell nucleus $^{144}$Sm to the strongly deformed $^{154}$Sm, $^{90}$Zr and $^{96}$Zr are both spherical nuclei. This suggests that the behavior may be associated more with going from neutron-poor to neutron-rich nuclei than from changing deformation.

Examples showing very large deviations in $a$ from the dashed line are the $^{28}$Si+$^{144}$Sm [46] and $^{40}$Ca+$^{124}$Sn [32] reactions. For the first reaction ($Z_1Z_2=868$) $V_B$ and $r_0(\text{expt})/r_0(\text{MAW})$ are high while $a$ is much lower than the trend value, similar to the $^{16}$O+$^{144}$Sm case. On the other hand the $^{40}$Ca+$^{124}$Sn reaction ($Z_1Z_2=1000$) shows the opposite behavior.

To quantify the relative neutron richness of nuclei, we define $\delta N$ to be the difference between the neutron number of a given isotope and the average neutron number of the stable odd-mass isotopes of the same element. The $\delta N$ values for $^{144}$Sm, $^{148}$Sm, and $^{154}$Sm are −4, 0, and +6, respectively. Those for $^{90}$Zr and $^{96}$Zr are −1 and +5, respectively, while $^{124}$Sn has a value of $\delta N$ of +7. For the projectiles, values of $\delta N$ are −1 for $^{16}$O and $^{28}$Si, +3 for $^{36}$S, and −3 for $^{40}$Ca. Thus all these cases suggest that the behavior may be associated with the neutron richness or poverty of the target and possibly of the projectile. It should be noted that a reaction between a very neutron-rich target and neutron-deficient projectile will necessarily involve multineutron transfer with positive $Q$ values. Examples are the $^{40}$Ca+$^{96}$Zr reaction (up to six neutrons) and the $^{24}$Ca+$^{124}$Sn reaction (up to eight neutrons).

However, it is necessary to point out that the reactions $^{40}$Ca+$^{192}$Sn ($\delta N=+4$), $^{194}$Pt ($\delta N=-1$) also allow transfer of up to eight neutrons yet do not show similar behavior to the $^{40}$Ca+$^{96}$Zr, $^{124}$Sn reactions. Further, the $^{40}$Ca induced reactions on $^{46,48,50}$Ti show the opposite behavior to the $^{16}$O+$^{144,148,154}$Sm reactions in respect of the differences between the Denisov and experimental values of $V_B$, and no significant variation in $a$.

There seems no doubt regarding the general increase of both $V_B(\text{Den})-V_B(\text{expt})$ and of $a$ with increasing $Z_1Z_2$. However, there are significant doubts when comparing more detailed behavior because data of varying quality have been obtained from a number of groups. It would be well worthwhile if the high energy cross sections were remeasured by a single group using detectors with near 100% efficiency. Substantial uncertainties can result from large uncertainties in the detection efficiencies; for the purpose of this analysis it is unfortunate that the data were obtained from barrier distribution measurements where *absolute* cross sections do not require high accuracy. It is also very important that the beam energies are determined in an accurate and consistent way, and this may differ between groups. If such remeasurements were done it should be possible to reduce fluctuations due to experimental uncertainties and derive more definitive information on these more detailed but interesting questions.

### B. Dynamical effects

A number of recent theoretical papers, which may be relevant to our results, will now be considered. Wang *et al.* [47,48] have used their "improved quantum molecular dynamics model" to study the fusion of neutron-rich nuclei, in particular for the reactions $^{40,48}$Ca+$^{90,96}$Zr, of which $^{40}$Ca+$^{90,96}$Zr have been studied experimentally [45]. They conclude that when nuclei, particularly those that are neutron rich, come close together a flow of neutrons occurs between them, resulting in a neck. The effect of a neck is to reduce the barrier (dynamical barrier) relative to the normal static fusion barrier between the two nuclei [49]. A similar effect has been seen in calculations using mean-field transport theory [50] in a study of the fusion of the symmetrical systems $^{16}$O+$^{16}$O and $^{58}$Ni+$^{58}$Ni. The reduction in the barrier is largest for bombarding energies below the static barrier, decreasing as the energy increases above the barrier. The result is to enhance the sub-barrier fusion cross sections over those calculated for a static barrier and, to a lesser extent, the above-barrier cross sections. Also, the more neutron rich the participants, the larger the separation distance at which they fuse and the thinner the dynamical barrier. A consequence of the fusion barrier increasing with increasing bombarding energy is that the slope of the above-barrier cross sections as a function of energy is reduced, thus providing a reason for a larger value of the parameter $a$.

In Ref. [47] Wang *et al.* obtain good fits to the experimental data for the $^{40}$Ca+$^{90,96}$Zr reactions. However, nuclear structure effects, such as those of the strengths and energies of the $3_1^-$ states, important in coupled channels calculations of sub-barrier fusion cross sections, are not included in their model.

One prediction from this model [47] is that the neutron-rich reactions $^{48}$Ca+$^{90}$Zr and $^{48}$Ca+$^{96}$Zr should show even stronger effects, such as sub-barrier enhancement, than the $^{40}$Ca+$^{96}$Zr reaction. It would be of great interest to measure these fusion reactions to see whether this prediction is fulfilled. However, there must be some doubt as to whether it would be, in view of the experimental results for the reactions $^{48}$Ca+$^{48}$Ca and $^{40}$Ca+$^{48}$Ca [51]. The $^{40}$Ca+$^{48}$Ca reaction shows considerable sub-barrier enhancement but the even more neutron-rich $^{48}$Ca+$^{48}$Ca reaction shows very little. An important difference between these two cases is that two or four positive $Q$-value neutron transfers can occur in the $^{40}$Ca induced reaction whereas all neutron transfers have negative $Q$ values in the $^{48}$Ca induced reaction. It does seem plausible that neutron transfer and consequent neck formation might be facilitated when the $Q$ values are positive.

Zagrebaev [52] has presented a model, incorporating neutron transfer, which gives good fits to the $^{40,48}$Ca+$^{48}$Ca, $^{48}$Ca+$^{90,96}$Zr and the $^{18}$O+$^{58}$Ni and the $^{16}$O+$^{60}$Ni [53] experimental data. It is claimed that transfer with negative $Q$ value has no effect on sub-barrier fusion enhancement. For the $^{40}$Ca+$^{48}$Ca case the calculated barrier distribution, including transfer, is very asymmetric with a very long high energy tail extending well beyond the no-coupling fusion barrier. This suggests that the above-barrier cross sections, and hence the value of $a$ derived from above-barrier fits, may be significantly affected.

There appears to be some conflict between the calculations related to the neutron richness of the participants [47] and those concerned with neutron-transfer reactions with positive $Q$ values [52] which needs to be resolved. Nevertheless, it is possible that both, which implicitly involve production of a neutron neck, might have some influence on the

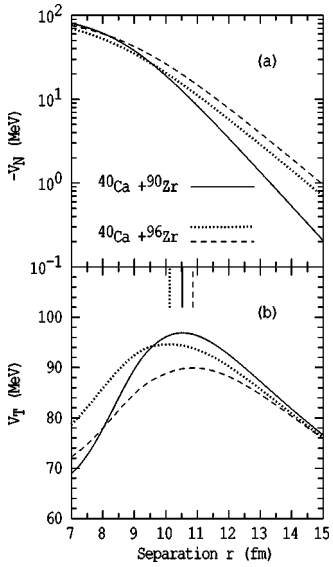


FIG. 13. (a) Nuclear ($V_N$) and (b) total ($V_T$) potentials derived from above-barrier fits to fusion data for the reactions $^{40}$Ca+$^{90}$Zr (full lines) and $^{40}$Ca+$^{96}$Zr (dotted lines). The dashed lines show the potentials for the $^{40}$Ca+$^{96}$Zr reaction where the value of $r_0$ has been changed to that for the $^{40}$Ca+$^{90}$Zr reaction. The barrier radii for these potentials are indicated by the vertical lines in (b).

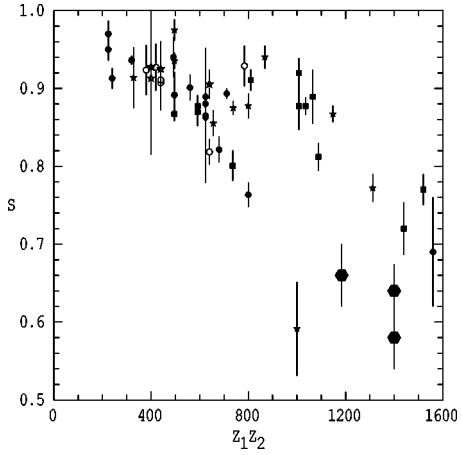


FIG. 14. Calculated suppression factors $S$ with respect to the MAW potential (see text). Symbols are as in Figs. 7 and 8, except that the large filled hexagons refer to the reactions $^{58}$Ni+$^{112,124}$Sn [56] and $^{32}$Si+$^{182}$W [57].

deduced values of the parameter $a$. Further, more detailed calculations are required to see whether this is indeed the case and, if so, how much of the observed increase in $a$ with $Z_1Z_2$ is acccounted for by this effect.

### C. Validity of static-potential approach

The nuclear and total potentials derived from fits to the experimental fusion cross sections for the $^{40}$Ca+$^{90}$Zr (solid lines) and $^{40}$Ca+$^{96}$Zr (dotted lines) reactions are shown in Figs. 13(a) and 13(b). The thicker barrier, leading to a larger value of the parameter $a$ and also the reduced value for $V_B$, is evident for the $^{96}$Zr case. There is no obvious physical reason why the value of the parameter $r_0$ should change from 1.073 fm for the $^{90}$Zr case to 1.017 fm for the $^{96}$Zr case. The dashed lines show the potentials when the value of $r_0$ for the $^{40}$Ca+$^{96}$Zr reaction is changed to be the same as that for the $^{40}$Ca+$^{90}$Zr reaction, the other parameters remaining the same. The value of $V_B$ is reduced by about 4.5 MeV, in gross disagreement with experiment. Further, none of these potentials would give good fits to elastic scattering data, which require a much smaller value for $a$. This suggests that, within this approach, the Woods-Saxon potential is not really appropriate for describing fusion reactions but that the parameters can be somewhat arbitrarily adjusted so that the values for $V_B$, $R_B$, and $\hbar\omega$ are appropriate for fitting the above-barrier fusion data. It was proposed in Ref. [54] that a potential with a Gaussian type falloff might fit both fusion and elastic scattering data. Although this form of potential is arbitrary it indicates that it might be possible to find a static potential which achieves this result. However, as indicated in Sec. I, present theories, such as the double-folding model [15,16], which do not include dynamical effects, do not support a potential with a Gaussian falloff.

### D. Possible effect of deep-inelastic scattering

A further possible explaination for the large values of $a$ arises because of the close, though not exact, relationship between the value of $\epsilon$ and the parameter $a$, as evidenced in Figs. 6 and 11. Even if $\epsilon=1.0$ it might be the case that the fusion cross section is depleted by some mechanism [for example, deep-inelastic collisions (DIC)]. This depletion certainly happens with the reaction $^{9}$Be+$^{208}$Pb [43], where the loosely bound $^{9}$Be has a significant chance of being broken up by the nuclear field before contact occurs [44]. Here one can say that complete fusion is suppressed by a factor $S$, which in this case has a value of 0.68 [43]. Provided that $S$ is independent of bombarding energy it can therefore be taken as equivalent to $\epsilon$. Possibly, similar incomplete fusion reactions may occur with other projectiles. Processes such as quasifission or deep-inelastic collisions may also deplete fusion in reactions with other projectiles. However, in order to produce a suppression, it would be necessary that in the measurement these products were excluded from the events identified as fusion. For heavier projectiles, it is likely that in most measurements incomplete fusion and quasifission, would be included in the fusion (capture) cross sections.

Assuming that the large empirical diffuseness values arise from fusion depletion, values of $S$ were determined, by taking the ratios of the measured capture cross sections to those calculated using the MAW potential (slightly adjusted to give the experimental value for $V_B$). They are shown in Fig. 14 as a function of $Z_1Z_2$. The data show a consistent downward trend with increasing $Z_1Z_2$, displaying considerable scatter, as did the empirical $a$ values. The deviation of $S$ from unity should exactly mirror the deviation of $a$ from the values of the MAW potential (solid line in Fig. 12), since a linear scaling of cross sections is part of both fitting procedures.

Also shown in Fig. 14 are three points (large filled hexagons), two at $Z_1Z_2=1400$ for the reactions $^{58}$Ni+$^{112,124}$Sn [55,56] and one at $Z_1Z_2=1168$ for the reaction $^{32}$S+$^{182}$W [57]. Both show very significant contributions from DIC at energies close to the fusion barrier, while Wolfs [55,56] found that this was so even at energies below the barrier. The value of $S$ has been taken as $\sigma_{\rm fus}/[\sigma_{\rm fus}+\sigma_{\rm DIC}]$, averaged over cases where $\sigma_{\rm fus}>200$ mb, where $\sigma_{\rm DIC}$ is the cross section for DIC. Wolfs' values of $[\sigma_{\rm fus}+\sigma_{\rm DIC}]$ were well reproduced [58] by a barrier passing calculation using the Bass potential and a 5% radius fluctuation, suggesting that indeed DIC are taking flux away from fusion.

This approach is also supported by a calculation by Dasso and Pollarolo [59], using a friction model, including fluctuations due to quantal zero-point motion of the collective modes, which gave fair agreement with Wolfs' results, and by the Langevin type calculations of Fröbrich and Marten [60–62], not including the quantal fluctuations, which gave similar agreement. The three points do not seem inconsistent with the other points with large $Z_1Z_2$ in Fig. 14. A more recent paper [63] has shown DIC similar in magnitude to those seen by Wolfs for the reactions $^{124,136}$Ni+$^{56,64}$Ni in the barrier region also. Unfortunately, the $\sigma_{\rm fus}$ were not measured in this case so that values for $S$ cannot be determined.

Most studies of DIC have been made at energies well above the barrier and it was a surprise when Wolfs found a significant DIC cross section near and below the barrier. Strongly damped reactions similar to DIC are reported to occur in lighter systems, for example, $^{32}$S+$^{64}$Ni [64] ($Z_1Z_2=448$) at energies well above the barrier. It would be interesting to see if they also occur at energies closer to the barrier. If they do, the values of $S$ might be reduced below unity and result in at least a partial explanation of the values for $a$, obtained from fitting the experimental data, being much larger than those deduced from the MAW potential. Deep-inelastic scattering might be expected to increase with $Z_1Z_2$ and thus may provide an explaination of the increase of the parameter $a$ with $Z_1Z_2$. The extra-push model of Swiatecki [26,27] includes in a schematic way both DIC and quasi fission. The predictions of this model for the reaction $^{19}$F+$^{208}$Pb are shown by the dash-dotted line in Fig. 2. This was calculated with the code of Back [27] and adjusted to give the experimental value of $V_B$. It gives a value for $a$ of 0.67 fm, when analyzed by our procedure. Calculations with this model give an approximately constant value for $a$, similar to that for the MAW potential, for lower values of $Z_1Z_2$, and then a rather sudden and drastic increase to values $>2$ fm when DIC become significant. Calculations with different models involving friction, similar to those reported above [59–62] but for lighter systems, would also be of great interest, especially as experimental measurements are likely to be difficult when $S$ approaches unity.

## V. CONCLUSIONS

A total of 46 fusion excitation functions, at energies above their average fusion barriers, have been analyzed, using Woods-Saxon potentials, to obtain values for the diffuseness parameters $a$, the nuclear potential radii $r_0$, and the fusion barriers $V_B$. The results were compared with those from the "bare" potentials of Denisov [34] and of Akyüz and Winther modified to Woods-Saxon form [13] and 100 MeV depth. In most cases the values of $r_0({\rm expt})/r_0({\rm MAW})$ appeared to be independent of $Z_1Z_2$, lying about an average value with a standard deviation of about 2.5%.

The experimental values of $V_B$ were consistently lower than those from Denisov's potential (and also the Akyüz-Winther potential), the difference increasing with increasing $Z_1Z_2$. Large deviations from the trend line occurred in a few cases. Experimental fusion barriers are expected be lower than those calculated with a bare potential because coupling to highly excited states (which increases with $Z_1Z_2$) reduces the barriers. Coupled channels calculations showed that the isoscalar giant-quadrupole resonance could account for up to 1/3 of the effect, and presumably coupling to all giant resonances would account for more. Coupling to collective $3^-$ states which, unlike collective $2^+$ states, do not show a strong correlation between strength and excitation energy, might cause fluctuations about the trend line.

The most important finding of this work is that the empirical diffuseness parameters $a$ determined by our fitting procedure are all considerably greater than those from the original or modified Akyüz-Winther potential. This may indicate that the WS form of nuclear potential is not appropriate in the barrier region, but it could also result from dynamical effects not included in the model used to fit the data. The deduced values for $a$ show a strong increase with increasing $Z_1Z_2$, albeit with fluctuations about the trend line. The complete data set does not show a consistent difference between results for closed-shell, vibrational, and deformed nuclei. The data do, however, suggest some correlation with the neutron richness of the projectile and target nuclei, those which are neutron rich tending to give larger values of $a$. Corresponding effects occur with the values of $V_B$. Recent theoretical calculations [47,48,50,52], suggesting or implying neutron-neck formation, give some support to these observations and for the neccessity of dynamical, rather than static-potential, calculations to explain the enigma of the large values for $a$.

A further possible contribution to the large values for $a$ might arise from the presence of damped reactions such as deep-inelastic scattering, which inhibit fusion. If correct it would again suggest the requirement for dynamical rather than static calculations. If it is assumed that fusion suppression due to DIC is the only reason for large $a$, the suppression of fusion for large $Z_1Z_2$ does not seem to be inconsistent with results for the reactions $^{58}$Ni+$^{112,124}$Sn and $^{32}$S+$^{182}$W, where DIC are known to occur (see Fig. 14). It would be interesting to study, both experimentally and theoretically, other cases with lower $Z_1Z_2$ near to the fusion barrier to see whether fusion was inhibited by the presence of DIC.

It is clear that the data, when interpreted with a static Woods-Saxon potential, require much larger values of $a$ than expected from elastic scattering or from the diffuseness of nuclear matter distributions. Some possible causes, based on the data and our current knowledge of fusion and reactions, are suggested. The systematics and the discussion are

presented here with the expectation that they will stimulate studies which incorporate physical effects that have been ignored in models of fusion thus far. Also, careful measurement of a large set of high energy cross sections, with a detector of near 100% efficiency, might help to resolve some of the experimental uncertainties associated with the present data set.

## ACKNOWLEDGMENTS

M.D. and D.J.H. acknowledge the support of an Australian Research Council Discovery Grant. We would like to thank J. S. Lilley, A. M. Stefanini, R. Vandenbosch, and J. X. Wei who kindly sent tables of their fusion cross sections.

[1] J. X. Wei, J. R. Leigh, D. J. Hinde, J. O. Newton, R. C. Lemmon, S. Elfström, and J. X. Chen, Phys. Rev. Lett. **67**, 3368 (1991).
[2] J. R. Leigh, M. Dasgupta, D. J. Hinde, J. C. Mein, C. R. Morton, R. C. Lemmon, J. P. Lestone, J. O. Newton, H. Timmers, J. X. Wei, and N. Rowley, Phys. Rev. C **52**, 3151 (1995).
[3] M. Dasgupta, D. J. Hinde, N. Rowley, and A. M. Stefanini, Annu. Rev. Nucl. Part. Sci. **48**, 401 (1998), and references therein.
[4] N. Rowley, G. R. Satchler, and P. H. Stelson Phys. Lett. B **254**, 25 (1991).
[5] C. H. Dasso and S. Landowne, Comput. Phys. Commun. **46**, 187 (1987).
[6] J. Fernández-Niello, C. H. Dasso, and S. Landowne Comput. Phys. Commun. **54**, 409 (1987).
[7] M. Dasgupta, A. Navin, Y. K. Agarwal, C. V. K. Baba, H. C. Jain, M. L. Jhingan, and A. Roy, Nucl. Phys. **A539**, 351 (1992).
[8] K. Hagino, N. Rowley, and A. T. Kruppa, Comput. Phys. Commun. **123**, 143 (1999).
[9] I. J. Thompson, Comput. Phys. Rep. **7**, 167 (1988). (Later versions such as FRXX include coupling to all orders in the nuclear coupling potential.)
[10] D. J. Hinde, C. R. Morton, M. Dasgupta, J. R. Leigh, J. C. Mein, and H. Timmers, Nucl. Phys. **A592**, 271 (1995).
[11] C. R. Morton, A. C. Berriman, M. Dasgupta, D. J. Hinde, J. O. Newton, K. Hagino, and I. J. Thompson, Phys. Rev. C **60**, 044608 (1999).
[12] Ó. Akyüz and A. Winther, in *Nuclear Structure and Heavy-Ion Physics*, Proceedings of the International School of Physics, "Enrico Fermi," Course LXXVII, Varenna, 1979, edited by R. A. Broglia, C. H. Dasso, and R. Richi (North-Holland, Amsterdam, 1981).
[13] R. A. Broglia and A. Winther, *Heavy Ion Reaction Lecture Notes, Volume I: Elastic and Inelastic Reactions* (Benjamin/Cummings, Reading, MA, 1981), p. 114.
[14] J. Blocki, R. Randrup, W. J. Swiatecki, and C. F. Tsang, Ann. Phys. (N.Y.) **105**, 427 (1977).
[15] K. Hagino, M. Dasgupta, I. I. Gonchar, D. J. Hinde, C. R. Morton, and J. O. Newton, *Proceedings of the Fourth Italy-Japan Symposium on Heavy-Ion Physics, Tokyo, Japan* (World Scientific, Singapore, 2002), pp. 87–98; nucl-th/0110065.
[16] I. I. Gontchar, M. Dasgupta, D. J. Hinde, and J. O. Newton, Phys. Rev. C **69**, 024610 (2004).
[17] J. O. Newton, R. D. Butt, M. Dasgupta, D. J. Hinde, I. I. Gontchar, C. R. Morton, and K. Hagino, Phys. Lett. B **586**, 219 (2004).
[18] C. L. Jiang, H. Esbesen, K. E. Rehm, B. B. Back, R. V. F. Janssens, J. A. Caggiano, P. Collon, J. Greene, A. M. Heinz, D. J. Henderson, I. Nishinaka, T. O. Pennington, and D. Seweryniak, Phys. Rev. Lett. **89**, 052701 (2002).
[19] C. L. Jiang, H. Esbesen, B. B. Back, R. V. F. Janssens, and K. E. Rehm, Phys. Rev. C **69**, 014604 (2004).
[20] M. Beckerman, J. Ball, H. Enge, M. Salomaa, A. Sperduto, S. Gazes, A. DiRienzo, and J. D. Molitoris, Phys. Rev. C **23**, 1581 (1981).
[21] J. G. Keller, K.-H. Schmidt, F. P. Hessberger, G. Münzenberg, and W. Reisdorf, Nucl. Phys. **A452**, 173 (1986).
[22] D. Ackermann, P. Bednarczyk, L. Corradi, D. R. Napoli, C. M. Petrache, P. Spolaore, A. M. Stefanini, K. M. Varier, H. Zhang, F. Scarlassara, S. Beghini, G. Montagnoli, L. Müller, G. F. Segato, F. Soramel, and C. Signorini, Nucl. Phys. **A609**, 91 (1996).
[23] K. Hagino, N. Rowley, and M. Dasgupta, Phys. Rev. C **67**, 054603 (2003).
[24] C. Y. Wong, Phys. Rev. Lett. **31**, 766 (1973).
[25] N. Rowley, A. Kabir, and R. J. Lindsay, J. Phys. G **15**, L269 (1989).
[26] W. J. Swiatecki, Phys. Scr. **24**, 113 (1981).
[27] B. B. Back, R. R. Betts, J. E. Gindler, B. D. Wilkins, S. Saini, M. B. Tsang, C. K. Gelbke, W. G. Lynch, M. A. McMahan, and P. A. Baisden, Phys. Rev. C **32**, 195 (1985).
[28] D. J. Hinde and M. Dasgupta, Prog. Theor. Phys. Suppl. (to be published).
[29] M. Dasgupta, D. J. Hinde, J. O. Newton, and K. Hagino, Prog. Theor. Phys. Suppl. (to be published).
[30] H. de Vries, C. W. de Jager, and C. de Vries, At. Data Nucl. Data Tables **36**, 495 (1987).
[31] J. X. Wei, J. R. Leigh, D. C. Weisser, J. O. Newton, S. Elfström, J. P. Lestone, J. X. Chen, D. G. Popescu, and D. J. Hinde, Nucl. Instrum. Methods Phys. Res. A **306**, 557 (1991).
[32] F. Scarlassara, S. Beghini, G. Montagnoli, G. F. Segato, D. Ackermann, L. Corradi, C. J. Lin, A. M. Stefanini, and L. F. Zheng, Nucl. Phys. **A672**, 99 (2000).
[33] A. M. Stefanini, L. Corradi, A. M. Vinodkumar, Yang Feng, F. Scarlassara, G. Montagnoli, S. Beghini, and M. Bisogno, Phys. Rev. C **62**, 014601 (2000).
[34] V. Yu. Denisov, Phys. Lett. B **526**, 315 (2002).
[35] K. Hagino, N. Takigawa, M. Dasgupta, D. J. Hinde, and J. R. Leigh, Phys. Rev. Lett. **79**, 2014 (1997).
[36] N. Takigawa, K. Hagino, M. Abe, and M. Balantekin, Phys. Rev. C **49**, 2630 (1994).
[37] S. Raman, C. W. Nestor, Jr., and K. H. Bhatt, Phys. Rev. C **37**, 805 (1988).
[38] R. H. Spear, At. Data Nucl. Data Tables **42**, 55 (1989).

[39] M. P. Metlay, J. L. Johnson, J. D. Canterbury, P. D. Cottle, C. W. Nestor, Jr., S. Raman, and V. G. Zelevinsky, Phys. Rev. C **52**, 1801 (1995).
[40] A. Van Der Woude, in *Giant Resonances*, edited by J. Speth (World Scientific, Singapore, 1990), Chap. 2.
[41] A. Bohr and B. R. Mottelson, *Nuclear Structure*, Vol. II (Benjamin, New York, 1975), p. 139.
[42] K. Hagino and N. Takigawa, Phys. Rev. C **58**, 2872 (1998).
[43] M. Dasgupta, D. J. Hinde, R. D. Butt, R. M. Anjos, A. C. Berriman, N. Carlin, P. R. S. Gomes, C. R. Morton, J. O. Newton, A. Szanto de Toledo, and K. Hagino, Phys. Rev. Lett. **82**, 1395 (1999).
[44] D. J. Hinde, M. Dasgupta, B. R. Fulton, C. R. Morton, R. J. Wooliscroft, A. C. Berriman, and K. Hagino, Phys. Rev. Lett. **89**, 272701 (2002).
[45] H. Timmers, D. Ackermann, S. Beghini, L. Corradi, J. H. He, G. Montagnoli, F. Scarlassara, A. M. Stefanini, and N. Rowley, Nucl. Phys. **A633**, 421 (1998).
[46] M. Dasgupta, D. J. Hinde, J. R. Leigh, R. C. Lemmon, J. C. Mein, C. R. Morton, J. O. Newton, and H. Timmers, in *Proceedings of the Workshop on Heavy-Ion Fusion, Padova, Italy* (World Scientific Press, Singapore, 1994), p. 115.
[47] Ning Wang, Xizhen Wu, and Zhuxia Li, Phys. Rev. C **67**, 024604 (2003).
[48] Ning Wang, Zhuxia Li, and Xizhen Wu, Phys. Rev. C **65**, 064608 (2002).
[49] A. Iwamoto and K. Harada, Z. Phys. A **326**, 201 (1987).
[50] V. N. Kodratyev, A. Bonasera, and A. Iwamoto, Phys. Rev. C **61**, 044613 (2000).
[51] M. Trotta, A. M. Stefanini, L. Corradi, A. Gadea, F. Scarlassara, S. Beghini, and G. Montagnoli, Phys. Rev. C **65**, 011601(R) (2001).
[52] V. I. Zagrebaev, Phys. Rev. C **67**, 061601(R) (2003).
[53] A. M. Borges, C. P. da Silva, D. Pereira, L. C. Chamon, E. S. Rossi, Jr., and C. E. Aguiar, Phys. Rev. C **46**, 2360 (1992).
[54] J. O. Newton, C. R. Morton, M. Dasgupta, J. R. Leigh, J. C. Mein, D. J. Hinde, H. Timmers, and K. Hagino, Phys. Rev. C **64**, 064608 (2001).
[55] F. L. H. Wolfs, W. Henning, K. E. Rehm, and J. P. Schiffer, Nucl. Phys. **196**, 113 (1987).
[56] F. L. H. Wolfs, Phys. Rev. C **36**, 1379 (1987).
[57] J. G. Keller, B. B. Back, G. G. Glagola, D. Henderson, S. B. Kaufman, S. J. Sanders, R. H. Siemssen, F. Videbaeck, B. D. Wilkins, and A. Worsham, Phys. Rev. C **36**, 1364 (1987).
[58] W. Reisdorf, J. Phys. G **20**, 1297 (1994).
[59] C. H. Dasso and G. Pollarolo, Phys. Rev. C **39**, 2073 (1989).
[60] P. Fröbrich and J. Marten, Z. Phys. A **339**, 171 (1991).
[61] J. Marten and P. Fröbrich, Nucl. Phys. **A545**, 854 (1992).
[62] P. Fröbrich and I. I. Gonchar, Phys. Rep. **292**, 131 (1998).
[63] J. Gehring, B. B. Back, K. C. Chan, M. Freer, D. Henderson, C. L. Jiang, K. E. Rehm, J. P. Schiffer, M. Wolansky, and A. H. Wuosmaa, Phys. Rev. C **55**, 2959 (1997).
[64] G. Russo, C. Agodi, R. Alba, M. Baldo, G. Bellia, R. Coniglione, A. Del Zoppo, P. Finocchiaro, Liu Jingyi, C. Maiolino, E. Migneco, P. Piattelli, A. Rapisarda, P. Sapienza, A. Brondi, V. Roca, G. Spadaccini, and F. Terrasi, Phys. Rev. C **39**, 2462 (1989).
[65] N. Keeley, J. S. Lilley, J. X. Wei, M. Dasgupta, D. J. Hinde, J. R. Leigh, J. C. Mein, C. R. Morton, H. Timmers, and N. Rowley, Nucl. Phys. **A628**, 1 (1998).
[66] V. Tripathi, L. T. Baby, J. J. Das, P. Sugathan, N. Madhavan, A. K. Sinha, P. V. Madhusudhana Rao, S. K. Hui, R. Singh, and K. Hagino, Phys. Rev. C **65**, 014614 (2001).
[67] A. A. Sonzogni, J. D. Bierman, M. P. Kelly, J. P. Lestone, J. F. Liang, and R. Vandenbosch, Phys. Rev. C **57**, 722 (1998).
[68] A. C. Berriman, D. J. Hinde, M. Dasgupta, C. R. Morton, R. D. Butt, and J. O. Newton, Nature (London) **413**, 144 (2001).
[69] C. E. Bemis, Jr., T. C. Awes, J. R. Beene, R. L. Ferguson, H. J. Kim, F. K. McGowan, F. E. Obenshain, F. Plasil, P. Jacobs, Z. Frankel, U. Smilanski, and I. Tserruya, ORNL Progress Report, 1986 (unpublished).
[70] A. Mukherjee, M. Dasgupta, D. J. Hinde, K. Hagino, J. R. Leigh, J. C. Mein, C. R. Morton, J. O. Newton, and H. Timmers, Phys. Rev. C **66**, 034607 (2002).
[71] A. C. Berriman, Ph.D thesis, Australian National University, 2001.
[72] D. J. Hinde, A. C. Berriman, M. Dasgupta, J. R. Leigh, J. C. Mein, C. R. Morton, and J. O. Newton, Phys. Rev. C **60**, 054602 (1999).
[73] A. M. Stefanini, D. Ackermann, L. Corradi, D. R. Napoli, C. Petrache, P. Spolaore, P. Bednarczyk, H. Q. Zhang, S. Beghini, G. Montagnoli, L. Mueller, F. Scarlassara, G. F. Segato, F. Soramel, and N. Rowley, Phys. Rev. Lett. **74**, 864 (1995).
[74] D. J. Hinde (private communication).
[75] R. D. Butt, D. J. Hinde, M. Dasgupta, A. C. Berriman, A. Mukherjee, C. R. Morton, and J. O. Newton, Phys. Rev. C **66**, 044601 (2002).
[76] C. R. Morton, A. C. Berriman, R. D. Butt, M. Dasgupta, A. Godley, D. J. Hinde, and J. O. Newton, Phys. Rev. C **62**, 024607 (2000).
[77] D. J. Hinde, A. C. Berriman, R. D. Butt, M. Dasgupta, C. R. Morton, A. Mukherjee, and J. O. Newton, Eur. Phys. J. A **13**, 149 (2002).
[78] J. D. Bierman, P. Chan, J. F. Lang, M. P. Kelley, A. A. Sonzogni, and R. Vandenbosch, Phys. Rev. C **54**, 3068 (1996).